

Modeling charge transport in Swept Charge Devices for X-ray spectroscopy

P. S. Athiray^{ab}, S. Narendranath^a, P. Sreekumar^a, J. Gow^c, V. Radhakrishna^a, B.R.S. Babu^{bd}

^aISRO Satellite Centre, Vimanapura, Bangalore, 560017 India

^bDepartment of Physics, University of Calicut, Kerala, India

^cPlanetary and Space Sciences Research Institute, The Open University, UK

^dDepartment of Physics, Sultan Qaboos University, Muscat

ABSTRACT

We present the formulation of an analytical model which simulates charge transport in Swept Charge Devices (SCDs) to understand the nature of the spectral redistribution function (SRF). We attempt to construct the energy-dependent and position dependent SRF by modeling the photon interaction, charge cloud generation and various loss mechanisms viz., recombination, partial charge collection and split events. The model will help in optimizing event selection, maximize event recovery and improve spectral modeling for Chandrayaan-2 (slated for launch in 2014). A proto-type physical model is developed and the algorithm along with its results are discussed in this paper.

Keywords: Swept Charge Device (SCD), Spectral Redistribution Function (SRF), C1XS, CLASS

1. INTRODUCTION

X-rays emitted from the Sun incident on the lunar surface interact with major rock forming elements, producing X-ray Fluorescence (XRF) emission. X-ray line energies and intensities of each are used to study the surface chemistry of the celestial object. Though similar technique was deployed in earlier missions starting from Apollo, the Chandrayaan-1 mission was optimally designed to generate the maximum coverage and generate the most spectroscopically accurate measure of major elemental abundance. The unusual low solar activity hampered completion of the primary scientific objective of Chandrayaan-1 X-ray Spectrometer (C1XS)¹ in creating a global lunar elemental map using XRF emission lines. Chandrayaan-2 Large Area Soft X-ray Spectrometer² (CLASS) is being developed for the upcoming mission Chandrayaan-2 (slated for launch in 2014) to complete the objective of global mapping of lunar surface chemistry. To achieve enhanced sensitivity to detect XRF emission lines from the Moon even during weak and quiescent solar conditions, CLASS is designed to have a total geometric area of 64 cm^2 using Swept Charge Device (CCD-236)³ developed by e2V Technologies Ltd., UK. It uses an array of 16 SCDs each with an area of 4 cm^2 .

Details about SCDs are described in Sec. 2 along with the architecture of CCD-54 which is modeled in the current work. Sec. 3 briefly covers the details of the charge transport in X-ray detectors along with assumptions used in our model. Understanding and interpretation of simulation results along with comparison with CCD-54 calibration data are discussed in Sec. 4. Summary of ongoing and future works are given in Sec. 5.

2. SWEPT CHARGE DEVICE (SCD)

SCD's are modified version of conventional two-dimensional X-ray CCD's. They can be considered as one-dimensional pseudo linear sensors developed exclusively for non-imaging, spectroscopic purposes. Through Multi-Pinned Phase mode operation and rapid continuous clocking, they provide high spectral resolution within benign operating temperature range of $-20 \text{ }^\circ\text{C}$ to $+5 \text{ }^\circ\text{C}$ for X-rays in the 0.5-10 keV range. The advantages of SCD over a conventional two-dimensional X-ray CCD are many: the reduction in read-out complexity, large collection area, good spectral resolution, minimal cooling requirement, suppression of surface generated dark current and avoidance of image integration period.

Further author information: (Send correspondence to P. S. Athiray)

P. S. Athiray: E-mail: athray@gmail.com, Telephone: +91 9901818170

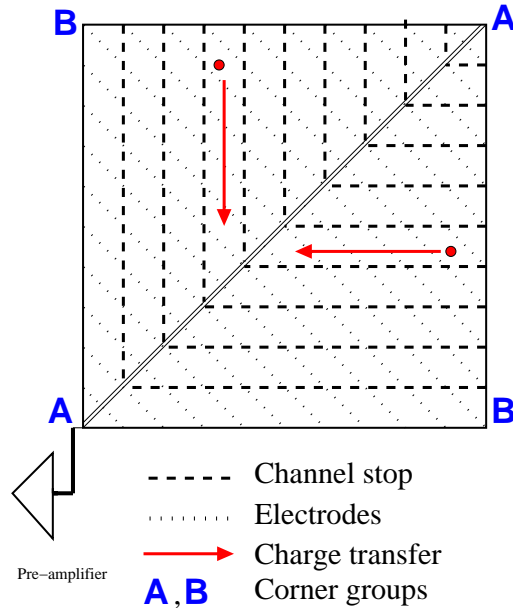


Figure 1. Schematic of CCD-54. The channel stops (dashed lines) and diagonal electrodes (dotted lines) are depicted respectively. Charge cloud produced by an X-ray photon will be clocked between the channel stops represented by a long arrow. Corners of SCD are grouped as A, B whose locations in the SCD are also marked.

2.1 SCD - CCD-54 - Architecture

CCD-54 consists of 1725 diagonal electrodes covering an active area of 1.07cm^2 including inbuilt buried channels. Schematic view of CCD-54 is shown in Fig. 1. Channel stops are fabricated in the epitaxial silicon wafer in the form of a herringbone structure. Charges produced in the underlying buried channel are clocked towards the diagonal transfer channel and then towards the readout amplifier. CCD-54 is configured for 3ϕ clocking and hence need 575 transfers to flush the complete device. A detailed description about the device is given in Lowe et al.⁴

2.2 Spectral Redistribution Function (SRF) of SCD's

Absorption of an X-ray photon in a detector results in a complex cascade of energy transfers. Energy deposited by the photon gets transformed in many ways leading to various signatures in the observed energy spectrum. The distribution of energy deposits observed in a device for an incident mono-energetic photon is called the spectral redistribution function (SRF). SRF strongly depends on the energy of the incident photon. It is observed that the SRF of SCD's exhibit four distinct features⁵ viz., a low energy tail, a low energy shelf, a low peak and escape peak in addition to the photopeak. Some of these feature arise due to the coupled action of diagonal readout and photon interaction at different depths in the SCD. Hence it is useful to have a detailed physical model to understand the SRF of SCD's from which contributions by each component can be derived. Development of a physical model of the SRF will help in:

1. Optimizing the logic for selection of events in SCD.
2. Recovering non-photopeak events which leads to a gain in the overall efficiency of the detector system.

Typically, SRF of pixellated detectors may be pixel position dependent. SRF of corner pixels differ significantly from the other pixels due to charge losses. We also study the pixel location dependency of SRF separately. For this purpose, the four corner pixels are grouped into two based on the similarity of SRFs. Group A contains two corner pixels which are (i) the one next to the readout amplifier and its diagonal counter part, marked as A in Fig. 1. The other two corner pixels form Group B (marked as B in Fig. 1).

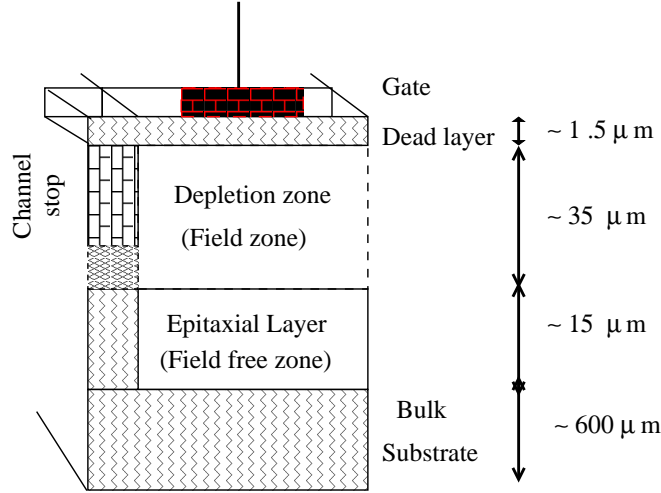


(Figure drawn not to scale)

Figure 2. The generic structure of CCD-54 device where photons are incident from the top. Interactions in the non-shaded layers are considered in the current model which contributes the most to the observed energy response. Approximate dimensions of different layers used in the code are taken from Narendranath et al.⁵

3. CHARGE TRANSPORT MODEL

The fundamental difference between a traditional X-ray CCD and SCD lie in its diagonal clocking readout structure.⁶ In CCD's, the amount of charge collected in each pixel due to photon interaction is preserved during the readout except for small charge transfer losses. In contrast, the diagonal charge transfer architecture of SCD allows charges from different areas of the device to get summed up at the diagonal prior to the final readout. Hence we first modeled a conventional 2-D X-ray CCD in our simulation over which we then incorporated the diagonal clocking readout mechanism of SCD.

3.1 Considerations in the model

The observed spectral response of SCD arises mainly from interactions at five different zones viz., channel stop, dead layer, field zone, field-free zone and bulk substrate. Channel stop occupies only a very tiny fractional area of the entire SCD (< few %). They are considered to be responsible for partial charge collection producing a low energy shelf. Total thickness of dead layer made up of multiple slabs (SiO_2 , Poly Si, Si_3N_4) in SCD is ≈ 1 to $2 \mu\text{m}$. Dead layer interaction contributing to the observed SRF becomes significant for low energy X-rays ($\leq 3 \text{ keV}$). X-ray photons with energies between 3-10 keV exhibit a maximum probability to interact in the field zone, field-free zone and bulk substrate. Predominant recombination and diffusion in the bulk zone due to very high doping concentrations ($N_a \approx 10^{18} \text{ cm}^{-3}$) will not allow the charge cloud to reach the collection gate. Hence in this work, we have modeled only photon interactions in the field and field-free zones. Photon interactions in the channel stop and dead layer are expected to be small.

We followed the approach adopted in simulating the response of Advanced Chandra Imaging Spectrometer (ACIS)⁷ and X-ray telescope (XRT) in Swift mission.⁸ We follow a Monte-Carlo based algorithm to simulate the interaction of mono-energetic X-ray photons in different layers of SCD. The aim of the model is to understand and quantify the non-photopeak events seen in the observed spectra. We attempt to model the photon interaction at different regions of CCD-54 both along the thickness and across the surface of the device. An algorithm is developed and code is written in Interactive Data Language (IDL). Global structure of SCD considered in the

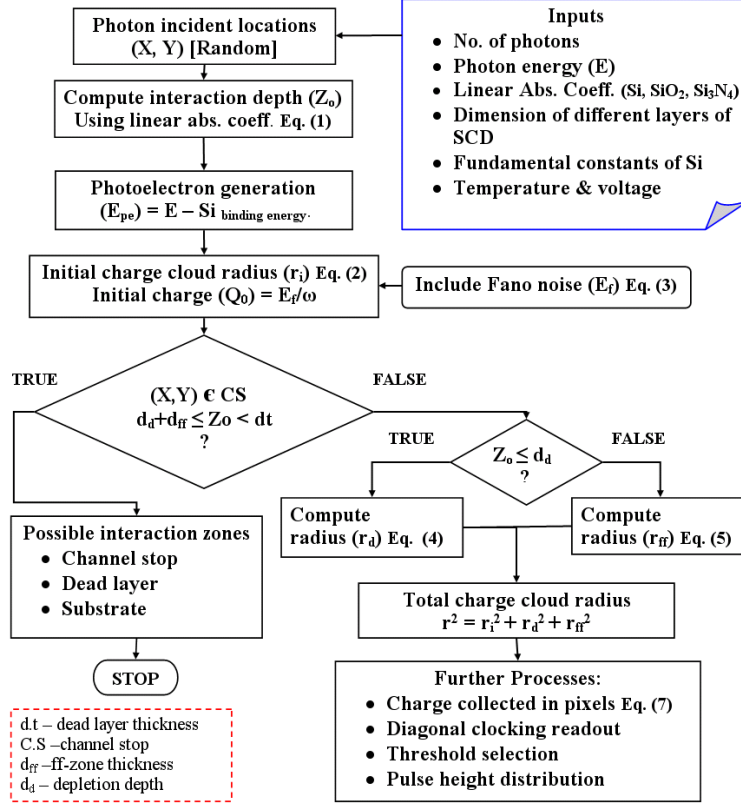


Figure 3. Flowchart explaining the architecture of charge transport model

present model with different component slabs arranged in order is shown in Fig. 2. A flowchart explaining the algorithm of current model is shown in Fig. 3.

3.2 Photon interactions

Photons are incident on the SCD from the top and travel through different layers before it interacts. Depending on the energy of incident X-ray photons the depth distribution at which interactions occur in the detector is computed by :

$$z_o = -\frac{1}{\mu(E)} \ln(R_u) \quad (1)$$

where $\mu(E)$ is the linear mass absorption coefficient of the material at photon energy E , R_u is a uniform random number. If the interaction depth is greater than the thickness of a slab, then the interaction depth is re-computed for the following slab. Absorption of an X-ray photon via photo-electric effect produces a photo-electron which on further ionization produces a charge cloud (e^- - h pairs). Initial radius (r_i) of this assumed spherical charge cloud is related to the energy of the photo-electron (E_{pe})⁹ :

$$r_i = \begin{cases} 40.0 \frac{E_{pe}^{1.75}}{\rho} & (5 \text{ keV} < E_{pe} < 25 \text{ keV}) \\ 30.9 \frac{E_{pe}^{1.53}}{\rho} & (E_{pe} \leq 5 \text{ keV}) \end{cases} \quad (2)$$

where ρ is the density of the detector material. It is also assumed that the radial charge profile of the initial charge cloud follows Gaussian distribution. In order to estimate the distribution of charge contained in the cloud,

Fano noise is added to the photon's energy using a normal random number generator which is given as :

$$E_f = E_i + R_n(0)\sqrt{F\omega E_i} \quad (3)$$

where E_f is the Energy distribution with Fano noise added, $R_n(0)$ is normal distributed random number with mean 0, F is the Fano factor and ω is the average energy required to produce an e^- -h pair.

3.2.1 Field & Field-free zone interactions

Interactions at depths (z_0) within the depletion zone are termed as field zone interactions. The negative charge cloud produced within the depletion depth (d_d) will experience the electric field and hence will drift towards the collection anode. Considering linear regime i.e., drift velocity \propto electric field, radius of the charge cloud (r_d) at the gate is computed after drifting through the depletion region.

Epitaxial region above the bulk substrate and below the depletion zone is called field-free zone. Due to the absence of electric field in this region, the charge cloud suffer from diffusion and recombination before it reaches the gate. Diffusion in field-free zone enlarges the radius of the charge cloud and causes spill over of charges across pixels. When charges are not contained within a pixel due to a photon hit, the events are called multi-pixel events or split events which are predominant for field-free zone interactions. It was clearly demonstrated by Pavlov et al.¹⁰ that the charge density distribution is non-Gaussian for field-free zone interactions.

For simplicity, we assume the charge cloud follows a Gaussian distribution and compute the radius of the charge cloud (r_{ff}) reaching the interface between field and field-free zone. Once the charge cloud reaches the boundary of field zone it drifts in the electric field and reaches the collection gate. Final radius (r) of the charge cloud at the gate is computed by taking the quadrature sum of r_i , r_d , r_{ff} from which the amount of charge collected in each pixel is derived. Standard fundamental equations used in the model for the computation of radius of charge clouds and charge collection in pixels are given in Appendix A. Values of some of the important parameters used in the model are listed in Table 1.

Table 1. Values of parameters used in modeling charge transport of CCD-54

Voltage (for d_d computation)	3.8 V
Temperature	263 K
Channel stop pitch	25 μ m
Number of acceptor impurities (N_a)	$4 \times 10^{12} cm^{-3}$
Number of pixels	25×25
Number of mono-energetic photons	3×10^4

4. RESPONSE SIMULATION

Using the algorithm described in Sec. 3, we simulated the SRF of SCD for multiple scenarios of photon interactions. In this section, we present the simulation results along with our understanding of the derived SRF. Simulations are performed for large number of different mono-energetic photons (4 keV, 4.51 keV, 5.0 keV, 6.0 keV and 8.0 keV). Simulations include interactions in (i) field zone and (ii) field-free zone at different pixel locations. As the laboratory calibration data are available at 4.51 keV (K_α of Ti), one of the simulation is performed at 4.51 keV.

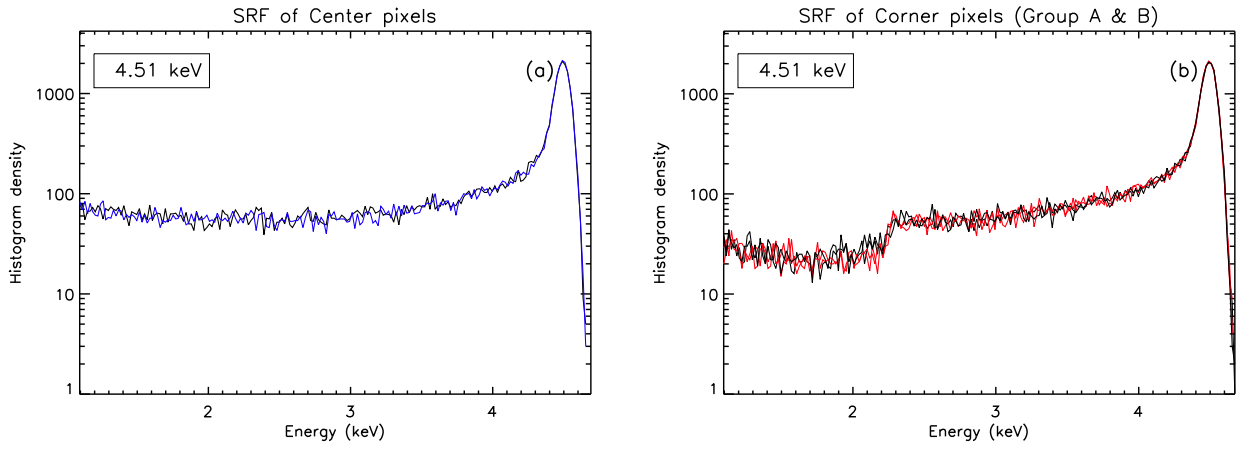


Figure 4. Simulated SRF of CCD-54 for 4.51 keV photons interacting in the field zone (a) photon incidence on center pixels (b) photon incidence on corner pixels (both group A (black) & B (red)). Photopeak and non-photopeak (low energy tail component) are clearly seen. The difference in the SRF is due to charge loss in the corner pixels which produces the dip seen in the low energy tail component.

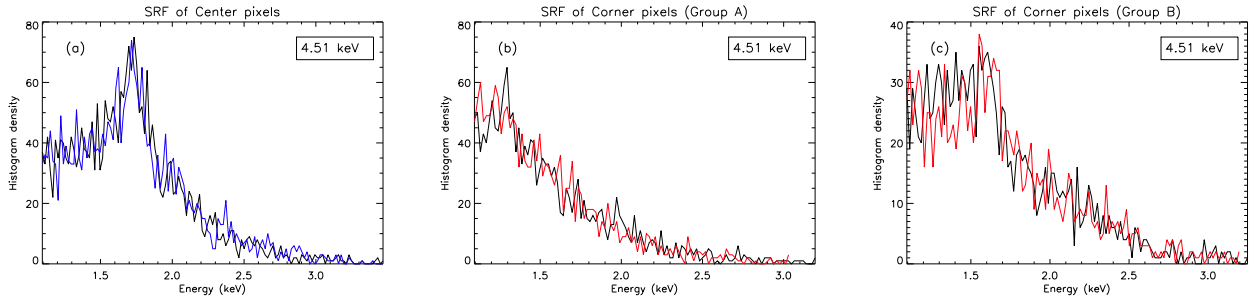


Figure 5. SRF of CCD-54 at 4.51 keV, simulated for interactions in field-free zone (a) photons incident on center pixels (b) photons incident on group A corner pixels (c) photons incident on group B corner pixels. Diagonal clocking of wide spread split events is responsible for this SRF. The difference in SRF between group A & B is mainly due to diagonal readout of diffused charges (i.e., unlike group B, group A pixels are along the diagonal readout). This clearly shows that field-free zone interactions contributes to the low energy peak component in the total SRF.

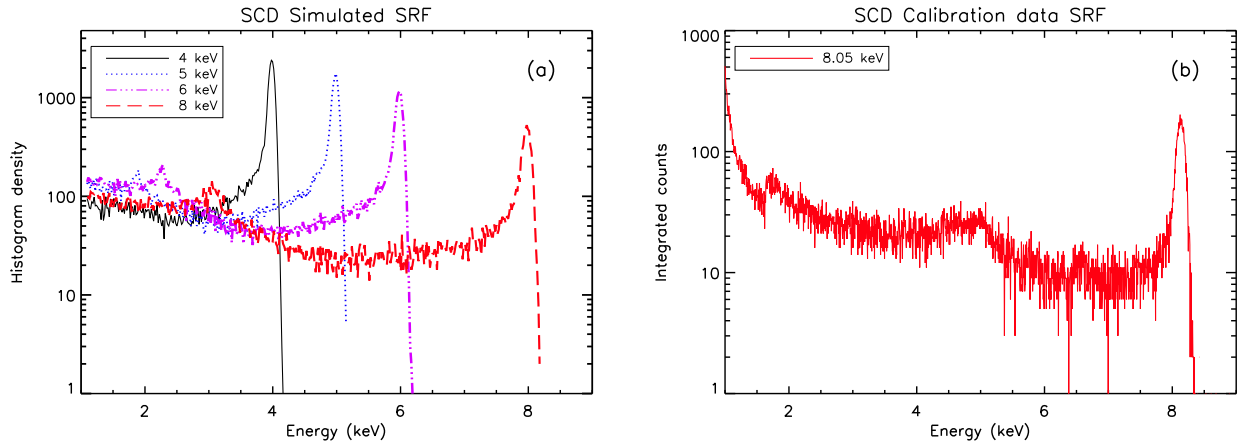


Figure 6. (a) SRF of CCD-54 simulated for different mono-energetic photons viz., 4 keV, 6 keV & 8 keV hitting a non-corner pixel in the detector (b) SRF at 8.05 keV of CCD-54 measured during C1XS calibration. Major SRF components viz., photopeak, low energy tail and low energy peak are clearly seen in both the cases.

4.1 Pixel dependency in Field zone

Energy spectrum of photons interacting only inside the depletion depth are discussed here. We also examine the SRF dependence for corner and central pixels separately. Results of simulation using 4.51 keV X-rays are shown in Fig. 4. For non-corner pixels, the SRF in this zone is characterized by a dominant photopeak (most of the charge produced is swept-up by the anode) and a low-energy tail. The low-energy tail contribution arises from charge splitting due to interactions at pixel boundaries and interactions at greater depths. Due to charge loss in the corner pixels (both group A & B), its SRFs differ by the presence of a dip in the tail at low energies as shown in Fig. 4(b).

4.2 Pixel dependency in Field-free zone

Photon interaction in field-free zone is more complex. The charge cloud diffuses into multiple pixels with some of the charges lost due to recombination. The spectrum thus has a low energy distribution without a photopeak. Energy response generated due to the interactions in central pixels for 4.51 keV X-rays producing non-photopeak events are shown in Fig. 5(a). SRF of corner pixels from group A and B differ from each other as shown in Figs. 5(b) & 5(c). This difference in SRF could be because, the multi-pixel events due to diffusion in group A are in line with the diagonal readout which is not the case for group B. From Figs. 5(a, b, c) it is clear that the low energy peak component in the SRF is produced by the photon interactions in field-free zone.

4.3 Energy dependency

Here we present the energy dependence of SRF (i.e., 4 keV, 5 keV, 6 keV and 8 keV). Derived SRF containing the photopeak and non-photopeak events (low energy tail and low energy peak) for X-rays incident on a center pixel are shown in Fig. 6. Features seen in the SRF are due to the combined response from field and field-free zone interactions. High energy X-ray photons penetrate deep inside the detector before interaction. Hence more interactions occur very deep in the field zone and in often diffuse into the field-free zone causing more split events. The expected trend of increase in photopeak and decrease in off-peak events with decrease in X-ray energies is clearly seen. Fig. 6(b) shows the spectrum of Cu K_{α} (8.05 keV) measured with CCD-54 during C1XS ground calibration tests at the RESIK facility, Rutherford Appleton Laboratory (RAL), UK. It is obvious from these plots that the profile of the derived SRF from our current model reproduces fairly well the calibration data. Figure 7(a) and 7(b) establishes the similarity in the variation of off-peak component with energy between the derived SRF and that obtained from laboratory calibration.

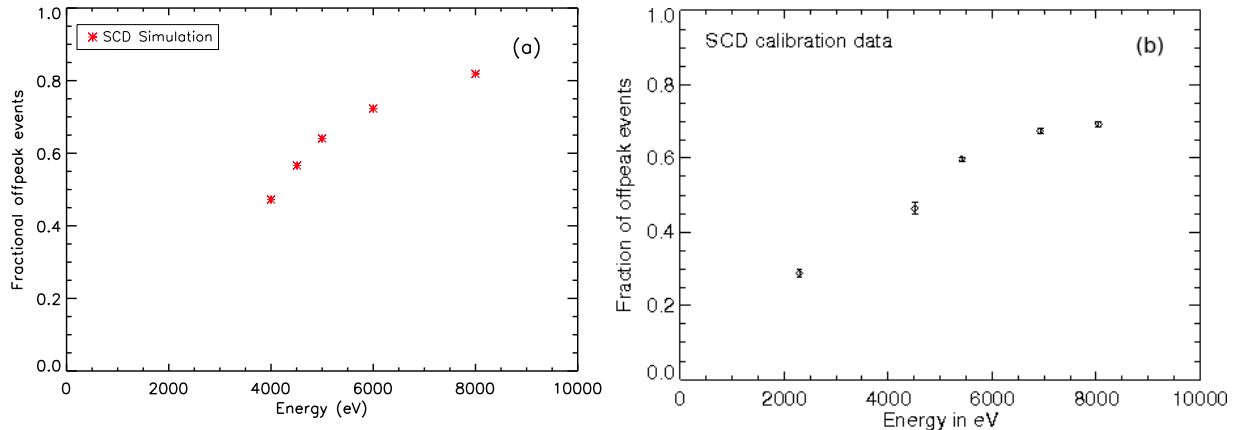


Figure 7. Variation of the off peak fractions in the SRF of CCD-54 as a function of energy is plotted (a) simulation (b) calibration data. The discrepancy between the data and the model suggest to make refinements in the model.

Calibration data shows that at 8.05 keV $\approx 75\%$ of total events are non-photopeak events. While simulation result yields $\approx 82\%$ contribution for the non-photopeak events in the total spectrum at 8keV. The discrepancy could arise from non-inclusion of interactions in other zones such as channel stop and also from assumption of ideal defect-free material in the simulation model. Currently simulations are performed only with small number of pixels and not with the exact threshold logic employed in C1XS. Inclusion of interactions in dead layers, channel stop, exact number of pixels and dimensions are all needed to establish a one-to-one comparison between the two.

5. ONGOING AND FUTURE WORK

It is inferred from this work that the proto-type model we have developed is promising and can give better insights about charge transport in SCDs. A physical interpretation is given for the major features in the SRF i.e., photopeak, and non-photopeak events (low energy tail & low energy peak) (4 keV - 10 keV). The differences observed here clearly suggest the need for further improvements in the current charge transport model. Post model revisions, we plan to implement the event selection logic used in C1XS to validate the model against data obtained during extensive C1XS calibration. After validation, we will incorporate the structure of CCD-236 with appropriate pixel dimensions in-order to generate its SRF. Extensive tests are planned with CLASS to generate adequate laboratory data on the dependencies of SRF using CCD-236.

APPENDIX A. EQUATIONS FOR FIELD & FIELD-FREE ZONE INTERACTIONS

Equation used to compute the radius of charge cloud reaching the collection node after drifting in the electric field is given by¹¹

$$r_f = 1 \times 10^4 \sqrt{\frac{4KT\epsilon}{e^2 N_a} \ln \left(\frac{d_d}{d_d - z_0} \right)} \quad (4)$$

where K is the Boltzmann constant, T is the temperature (in K), ϵ is the electric permittivity of silicon, e is the charge of an electron and N_a is number density of acceptor impurities. For interaction in the epitaxial field-free zone ($z_0 > d_d$), we assumed that no charge enters into the bottom substrate layer i.e., charges are reflected back at the boundary between field-free and substrate layer. We also assumed that recombination is negligible as $L \gg d_{ff}$. Equation to compute the radius of charge cloud at the interface between field-free and field zone is¹⁰ :

$$r_{ff} = \sqrt{2d_{ff}L \left[\tanh\left(\frac{d_{ff}}{L}\right) - \left(1 - \frac{z_0 - d_d}{d_{ff}}\right) \tanh\left(\frac{d_{ff} - z_0 + d_d}{L}\right) \right]} \quad (5)$$

where d_d is the depletion depth, z_0 is the interaction depth in the detector, d_{ff} is the thickness of epitaxial field free zone, L is the diffusion length.

Final radius of the charge cloud is given by :

$$r = \sqrt{r_i^2 + r_d^2 + r_{ff}^2} \quad (6)$$

Assuming Gaussian charge density profile for the cloud in both field and field-free zone cases, the equation to derive the amount of charges collected in each pixel (i,j) is given by Pavlov and Nousek:¹⁰

$$Q_{ij}(x_0, y_0) = \frac{Q_0}{4} \left[\operatorname{erf}\left(\frac{a_{i+1} - x_0}{r}\right) - \operatorname{erf}\left(\frac{a_i - x_0}{r}\right) \right] \left[\operatorname{erf}\left(\frac{b_{j+1} - y_0}{r}\right) - \operatorname{erf}\left(\frac{b_j - y_0}{r}\right) \right] \quad (7)$$

where Q_0 is the initial charge (E_f/ω), a and b are pixel dimensions, $a_i = -\frac{a}{2} + ia$, $b_j = -\frac{b}{2} + jb$ and r is given by Eq. 6. x_0, y_0 are photon interaction coordinates in a pixel where photon is absorbed with its origin at the pixel center (i.e., $-a/2 < x_0 < a/2$, $-b/2 < y_0 < b/2$).

REFERENCES

1. M. Grande et al., "The C1XS X-ray Spectrometer on Chandrayaan-1," *Planet. Space Sci.* **57**, pp. 717–724, 2009.
2. V. Radhakrishna et al., "The Chandrayaan2 Large Area Soft X-ray Spectrometer (CLASS)," in *42nd Lunar and Planet. Sci. Conf.*, Dorn, David A ed., *Proc. LPSC* **1608**, pp. 1708, 2011.
3. A. D. Holland and P. J. Pool, "A new family of swept charge devices (SCDs) for x-ray spectroscopy applications," in *High Energy, Optical, and Infrared Detectors for Astronomy III*, Dorn, David A ed., *Proc. SPIE* **7021**, pp. 702117, 2008.
4. B. G. Lowe, A. D. Holland, I. B. Hutchinson, D. J. Burt and P. J. Pool, "The sweptchargedevice, a novel CCD-based EDX detector: first results," *Nucl. Inst. Meth. Phys. Res. A* **458**, pp. 568–579, 2001.
5. S. Narendranath, P. Sreekumar, B. J. Maddison, C. J. Howe, B. J. Kellett, M. Wallner, C. Erd and S. Z. Weider, "Calibration of the C1XS instrument on Chandrayaan-1," *Nucl. Inst. Meth. Phys. Res. A* **621**, pp. 344–353, 2010.
6. J. Gow, *Radiation Damage Analysis of the Swept Charge Device for the C1XS Instrument*, Ph.D., Thesis, Brunel Univ., 2009.
7. L. K. Townsley, P. S. Broos, G. Chartas, E. Moskalenko, J. A. Nousek, G. G Pavlov, "Simulating CCDs for the Chandra Advanced CCD Imaging Spectrometer," *Nuc. Inst. Meth. Phys. Res. A*, **486**, pp. 716–750, 2002.
8. O. Godet, A. P. Beardmore, A. F. Abbey, J. P. Osborne, G. Cusumano, C. Pagani, M. Capalbi, M. Perri, K. L. Page, D. N. Burrows, S. Campana, J. E. Hill, J. A. Kennea and A. Moretti, "Modelling the spectral response of the Swift-XRT CCD camera: experience learnt from in-flight calibration," *Astron. Astroph.* **494**, pp. 775–797, 2009.
9. O. Kurniawan and V. K. S. Ong, "Investigation of Range-energy Relationships for Low-energy Electron Beams in Silicon and Gallium Nitride," *J. Scan. Elec. Micro.*, **29**, pp. 280–286, 2007.
10. George G. Pavlov and John A. Nousek, "Charge diffusion in CCD X-ray detectors," *Nucl. Inst. Meth. Phys. Res. A* **428**, pp. 348–366, 1999.
11. Gordon R. Hopkinson, "Analytic modeling of charge diffusion in charge-coupled-device imagers," *Opt. Eng.* **26**, pp. 766–772, 1987.